

RESEARCH ARTICLE

10.1029/2022MS003399

Key Points:

- A wavelet-based spectral method to estimate eddy variability is described
- Wavenumber spectra of eddies are estimated for a doubly periodic quasi-geostrophic flow
- The wavelet and Fourier approach agree well in their estimates of spectra and spectral flux

Correspondence to:

W. K. Dewar,
wdewar@fsu.edu

Citation:

Uchida, T., Jamet, Q., Poje, A. C., Wienders, N., Dewar, W. K., & Deremble, B. (2023). Wavelet-based wavenumber spectral estimate of eddy kinetic energy: Idealized quasi-geostrophic flow. *Journal of Advances in Modeling Earth Systems*, 15, e2022MS003399. <https://doi.org/10.1029/2022MS003399>

Received 8 SEP 2022
Accepted 10 MAR 2023

Author Contributions:

Conceptualization: William K. Dewar
Data curation: Takaya Uchida
Formal analysis: Takaya Uchida
Funding acquisition: William K. Dewar
Investigation: Takaya Uchida, Nico Wienders, William K. Dewar
Methodology: Takaya Uchida, William K. Dewar
Project Administration: William K. Dewar
Resources: William K. Dewar
Software: Takaya Uchida
Validation: Takaya Uchida, Quentin Jamet, Andrew C. Poje, William K. Dewar, Bruno Deremble
Visualization: Takaya Uchida
Writing – original draft: Takaya Uchida, William K. Dewar
Writing – review & editing: Quentin Jamet, Andrew C. Poje

© 2023 The Authors. Journal of Advances in Modeling Earth Systems published by Wiley Periodicals LLC on behalf of American Geophysical Union. This is an open access article under the terms of the [Creative Commons Attribution License](https://creativecommons.org/licenses/by/4.0/), which permits use, distribution and reproduction in any medium, provided the original work is properly cited.

Wavelet-Based Wavenumber Spectral Estimate of Eddy Kinetic Energy: Idealized Quasi-Geostrophic Flow

Takaya Uchida^{1,2} , Quentin Jamet^{2,3} , Andrew C. Poje⁴ , Nico Wienders⁵ , William K. Dewar^{2,5} , and Bruno Deremble² 

¹Center for Ocean-Atmospheric Prediction Studies (COAPS), Florida State University, Tallahassee, FL, USA, ²Université Grenoble Alpes, CNRS, INRAE, IRD, Grenoble INP, Institut des Géosciences de l'Environnement, Grenoble, France, ³INRIA, ODYSSEY group, Ifremer, Plouzané, France, ⁴Department of Mathematics, College of Staten Island, CUNY, New York, NY, USA, ⁵Department of Earth, Ocean and Atmospheric Science, Florida State University, Tallahassee, FL, USA

Abstract A wavelet-based method is re-introduced in an oceanographic and spectral context to estimate wavenumber spectrum and spectral flux of kinetic energy and enstrophy. We apply this to a numerical simulation of idealized, doubly periodic quasi-geostrophic flows, that is, the flow is constrained by the Coriolis force and vertical stratification. The double periodicity allows for a straightforward Fourier analysis as the baseline method. Our wavelet spectra agree well with the canonical Fourier approach but with the additional strengths of negating the necessity for the data to be periodic and being able to extract local anisotropies in the flow. Caution is warranted, however, when computing higher-order quantities, such as spectral flux.

Plain Language Summary Chaotic flows such as the ocean currents, atmospheric winds, and turbulence in general are fundamentally impossible to analytically predict, namely, to formulate a mathematical general solution. Nevertheless, the interest in describing such chaotic flows can be found in examples as old as Leonardo da Vinci's sketch of turbulence. While we cannot obtain an analytical description of turbulence, we can extract statistical information from turbulent flows and a common descriptor has been the wavenumber spectrum. The spectrum reveals at each spatial scale, the level of variability the flow carries. Here, we re-introduce an alternative method in estimating the spectrum based on wavelet functions.

1. Introduction

Fundamental to the goal of properly modeling climate system dynamics is understanding and quantifying how energy is both distributed, and ultimately transferred, across an extremely broad range of dynamically active space and time scales. In the atmospheric and ocean context, the most common means of quantifying the scale-dependent energy content of a chaotic, turbulent flow field is the energy spectrum (e.g., Charney, 1971; Kolmogorov, 1941; Nastrom & Gage, 1983; Taylor, 1938; Yaglom, 2004) given by the Fourier transform of two-point (spatial or temporal) velocity correlations.

We will focus in this paper on spatial correlations since the behavior of wavenumber spectra are described by “inertial range” theories predicting spectral slopes and cascades (Vallis, 2006). The standard Fourier approach has had great success in providing us with spectral estimates of energy partition (e.g., Ajayi et al., 2021; Stammer, 1997; Uchida et al., 2017; Xu & Fu, 2011, 2012) and its straightforward mathematical formulation facilitates the spectral interpretation in the original context, namely statistically homogeneous flows where Fourier decompositions are natural. Issues persist, however, in geophysical flows which are statistically inhomogeneous, anisotropic, and non-stationary (Uchida, Jamet, et al., 2021). The assumption of homogeneity lies on the fact that a Fourier transform is a global operator over the entire space-time domain of interest. In other words, the Fourier description of the field conflates different regimes of an inhomogeneous flow. A notable example is in the separated Gulf Stream region where the energetics have been argued to be distinct from the gyre interior (Jamet et al., 2021).

With a growing acknowledgment of the shortcomings of the Fourier approach, there has been a recent effort in the geophysical sciences to re-examine the cross-scale energetics. Notable examples are: (a) Aluie et al. (2018), Sadek and Aluie (2018), Schubert et al. (2020), Storer et al. (2022), Srinivasan et al. (2022), and Contreras et al. (2022) where they implement a spatial filter, (b) Lindborg (2015), Balwada et al. (2016, 2022), LaCasce (2016), Poje et al. (2017), and Pearson et al. (2020) where they use structure functions, (c) Jamet et al. (2020) where they employ the Green's function, and (d) Uchida, Jamet, et al. (2021) where they use Empirical Orthogonal Functions

all with the goal of examining the kinetic energy (KE) spectra and cross-scale transfer in the wavenumber domain. The overall consistent picture is that at scales about $O(100 \text{ km})$ where the oceanic motions are constrained by the Earth's rotation and vertical stratification, KE cascades upscale while KE on the scale of $O(10 \text{ km})$ tend to cascade downscale due to a loss of balance with the two constraining forces. While all these approaches, including the Fourier method, can capture within limits the spatial anisotropy when examined on a two-dimensional (2D) wavenumber plane, they lose this information when reduced to one-dimensional (1D) spectral quantities.

Here, we use a wavelet-based technique which yields localized pseudo-Fourier 1D wavenumber spectra capable of capturing the local anisotropies in the flow (Daubechies, 1992; Perrier et al., 1995). Wavelets emerged in the 1980s as a way to analyze time and space series in more local manner than was possible using Fourier techniques (e.g., Alvera-Azcárate et al., 2007; Doglioli et al., 2007; Thomson & Emery, 2014; Vasilyev & Paolucci, 1997), although strong parallels and connections are to be found between the two methods (Katul & Parlange, 1995; Torrence & Compo, 1998). We will argue the localized nature of wavelets allows us to capture the inhomogeneity and anisotropy in the flow (Farge, 1992; Horbury et al., 2008). We then apply the wavelet approach to estimate the horizontal KE and enstrophy spectral flux from a doubly periodic quasi-geostrophic (QG) flow, and to a flow subdomain where periodicity no longer applies. The comparisons illustrate some of the advantages of the wavelet approach.

The paper is organized as follows: We describe the QG model and provide an overview of the wavelet method in Section 2. Results are given in Section 3 where we compare our wavelet spectra to the canonical Fourier spectra. Conclusions are given in Section 4.

2. Theory and Technique

We describe the configuration of our QG model and provide an overview of the wavelet method.

2.1. Description of the Quasi-Geostrophic Simulation

We consider a stochastically forced two-layer QG flow in a doubly periodic f plane domain (i.e., $\beta = f_y = 0$) under rigid-lid and flat bottom conditions. Solutions to the QG potential vorticity (PV) equation

$$q_{jt} + \mathbf{J}(\psi_j, q_j) = -r_b \nabla^2 \psi_j \delta_{j,2} + \mathcal{Q} \quad (1)$$

are computed using the pseudo-spectral `pyqg` model (Abernathey et al., 2022), where δ_{ij} is the usual Kronecker delta function and layer numbers are denoted $j = 1, 2$. The linear bottom drag coefficient is $r_b = 5.787 \times 10^{-7} \text{ s}^{-1}$. The PV in each layer are

$$q_1 = \nabla^2 \psi_1 + F_1(\psi_2 - \psi_1), \quad (2)$$

$$q_2 = \nabla^2 \psi_2 + F_2(\psi_1 - \psi_2). \quad (3)$$

The vortex stretching coefficients are $F_1 = \frac{(2\pi/R_d)^2}{1+\delta}$, $F_2 = \delta F_1$ where the internal Rossby deformation radius was prescribed as $R_d = 100 \text{ km}$. Each layer thickness is $(H_1, H_2) = (500, 2,000) \text{ m}$ respectively, giving $\delta = H_1/H_2 = 0.25$. The square domain size is $L_0 = 1,000 \text{ km}$ with the spatial resolution of $\sim 2 \text{ km}$ (512×512 grid points). In order to prevent the system from equilibrating to the well-known single pair of positive and negative vortices (Vallis, 2006), a vertically uniform forcing was introduced as

$$\mathcal{Q} = A_q w(t, y, x), \quad (4)$$

where $A_q = 10^{-15} \text{ s}^{-2}$ is the amplitude and $w(t, y, x)$ is white noise in space-time with zero mean and $O(1)$ amplitude per layer (Figure 1). The quantity $w(t, y, x)$ was computed by taking the inverse Fourier transform of a ring in wavenumber space

$$\hat{w}(t, k^y, k^x) = \begin{cases} a(t, k^y, k^x) + ib(t, k^y, k^x), & \text{if } (R_d + \delta_R)^{-1} < \sqrt{k^x^2 + k^y^2} < (R_d - \delta_R)^{-1} \\ 0, & \text{otherwise} \end{cases}, \quad (5)$$

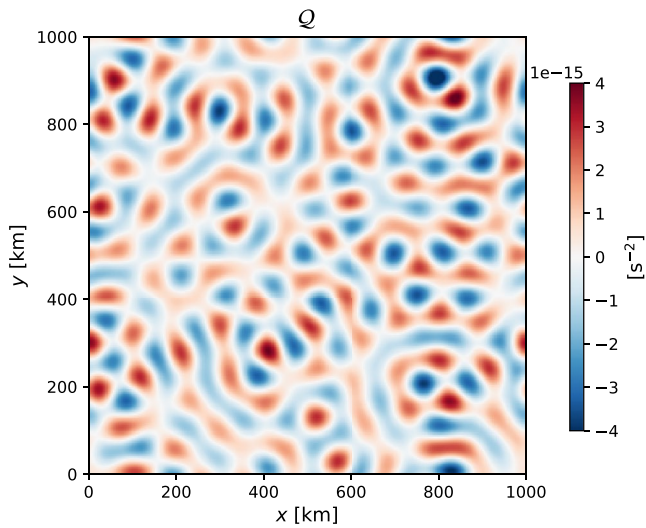


Figure 1. Example of how the vertically uniform stochastic forcing Q looks like for an arbitrary time step.

where k^x and k^y are the zonal and meridional wavenumbers, respectively, a and b are Gaussian random variables in the horizontal wavenumber space with zero mean and standard deviation of unity, and $\delta_R = 5$ km. After taking the inverse Fourier transform, the horizontal spatial mean is removed and then divided by the mean of the absolute values in the horizontal dimension in order to have the magnitude on the order of unity. In other words, the model is stochastically forced at scales about the Rossby radius uncorrelated in time. No background PV was prescribed. The model was spun up for 10 years from a state of rest, at which point area averaged energy had equilibrated (not shown), and then run for another 20 years with outputs saved every 10 days as instantaneous snapshots. The timeseries of the kinetic energy (KE, $K = (\mathbf{u} \cdot \mathbf{u})/2$) and potential energy (PE, $2(\psi_1 - \psi_2)^2/R_d^2$) for the 20 years of output are given in Figure 2, which mirror each other and roughly show an equipartition.

In this simple configuration, it is expected the flow will be both homogeneous and isotropic in the horizontal dimensions. Further, classical theory predicts the existence of an inverse cascade of KE and hence a $-5/3$ power law at scales larger than the forcing scale, and a forward cascade of enstrophy and hence -3 power law at smaller scales that are above the viscous dissipation scale (Vallis, 2006). In this sense, we “know” what the answer should be and can use the results to test the efficacy of the wavelet transform. The

double periodicity also allows for a straightforward comparison between the wavelet and Fourier approach as no windowing of the data is necessary in applying the transforms. We exhibit the top- and bottom-layer PV at the last time step of the model's 10th year in Figure 3.

2.2. Spectral Considerations

For the reasons outlined in the introduction, we depart from the classical Fourier approach to compute wavenumber spectra, but do note the utility of that wavenumber spectrum emerges largely from Parseval's equality

$$\int_{\mathbf{x}} K(\mathbf{x}) d\mathbf{x} = \int_{\mathbf{k}} \hat{E}_K(\mathbf{k}) d\mathbf{k}, \quad (6)$$

where $\mathbf{x} = (x, y)$, $\mathbf{k} = (k^x, k^y)$ (e.g., Capet et al., 2008; Scott & Wang, 2005; Uchida et al., 2017). The Fourier energy spectrum is given by $2\hat{E}_K(\mathbf{k}) = \hat{\mathbf{u}}^* \cdot \hat{\mathbf{u}}$ where the Fourier transform of the velocity is denoted by the hat ($\hat{\mathbf{u}}$) and the superscript $*$ denotes the complex conjugate. This equivalence of the area integrated KE to the wavenumber integrated Fourier spectrum motivates the latter's interpretation as the KE density in the wavenumber domain.

We base our spectral analysis on wavelet decompositions, rather than Fourier transforms, as the space-time locality of wavelets does not require the data to be periodic. Given a function dependent on two spatial dimensions, $f(\mathbf{x})$, its continuous wavelet transform is given by Daubechies (1992) and Torrence and Compo (1998)

$$\tilde{f}(s, \phi, \gamma) = \int_{\Omega} f(\mathbf{x}) \frac{1}{s} \xi^* \left(\mathbf{R}^{-1} \cdot \left(\frac{\mathbf{x} - \gamma}{s} \right) \right) d\mathbf{x}, \quad (7)$$

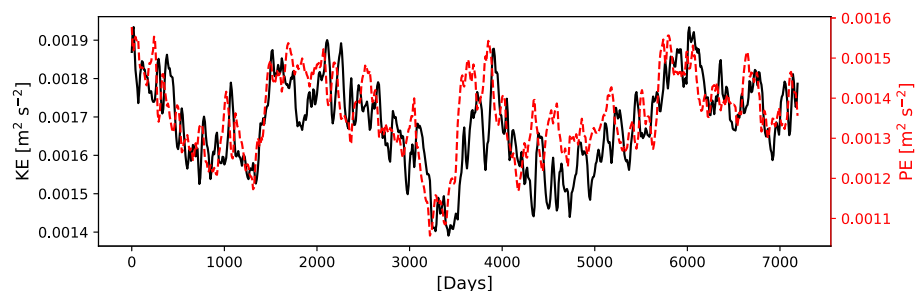


Figure 2. Vertically and domain averaged kinetic energy (black solid) and (available) potential energy (red dashed).

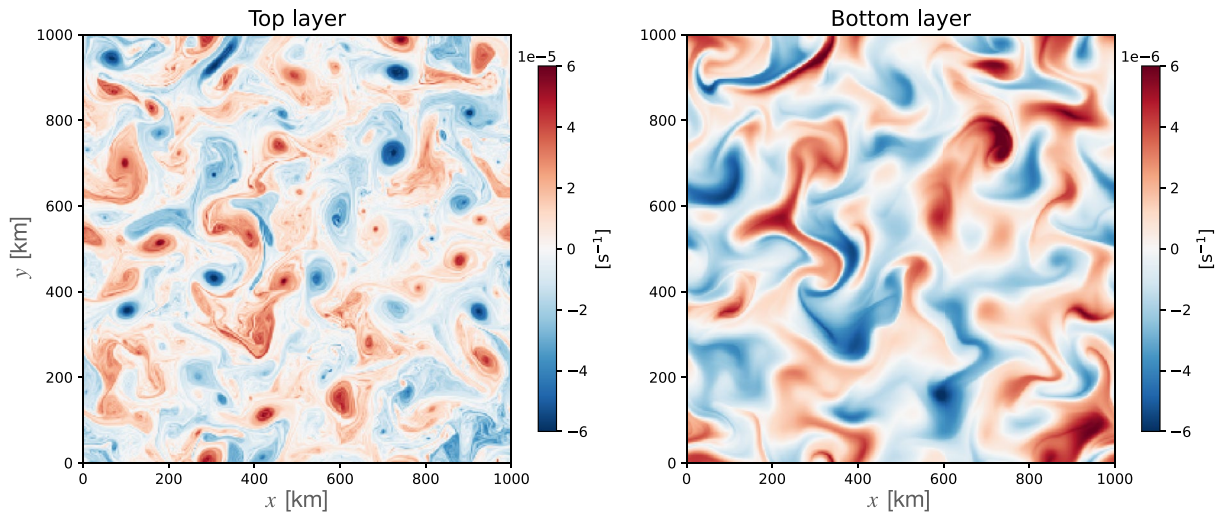


Figure 3. The potential vorticity at the last time step of the 10th simulated year in the top and bottom layer. Note the order of magnitude difference in the two panels.

where the integration is taken over the whole domain of interest Ω and \mathbf{R}^{-1} is the inverse of the rotation matrix

$$\mathbf{R}^{-1} = \begin{pmatrix} \cos(\phi) & \sin(\phi) \\ -\sin(\phi) & \cos(\phi) \end{pmatrix}, \quad (8)$$

for rotation through an angle ϕ relative to the x axis. The quantity s is referred to as the “scale,” $\gamma \in \mathbf{R}^2$ are the two-dimensional coordinates of interest, $\xi(\mathbf{x})$ is the so-called “mother” wavelet and $\xi(\mathbf{R}^{-1} \cdot (\mathbf{x} - \gamma)/s)$ in Equation 7 are the daughter wavelets. The quantities \tilde{f} are called the wavelet coefficients. Note that the field of wavelet coefficients is a filtered version of the original data.

Subject to the “admissibility condition” $C_{\Xi} < \infty$, the original function f can be reconstructed from the wavelet coefficients (Daubechies, 1992; Torrence & Compo, 1998)

$$f(\mathbf{x}) = \frac{1}{C_{\Xi}} \int_{\gamma} \int_s \int_{\phi} \tilde{f}(s, \phi, \gamma) \frac{1}{s^4} \xi\left(\mathbf{R}^{-1} \cdot \left(\frac{\mathbf{x} - \gamma}{s}\right)\right) d\phi ds d\gamma. \quad (9)$$

If $\hat{\Xi}(\mathbf{k})$ is the Fourier transform of the mother wavelet, then

$$C_{\Xi} = \int_{\mathbf{k}} \frac{\hat{\Xi}^* \hat{\Xi}}{\mathbf{k} \cdot \mathbf{k}} d\mathbf{k}. \quad (10)$$

The so-called “admissibility condition” implies that the mother wavelet defines a well-behaved class of wavelet transforms. Many functions satisfy Equation 10 provided they have zero mean

$$\int_{\mathbf{x}} \xi(\mathbf{x}) d\mathbf{x} = 0. \quad (11)$$

For current purposes, we will employ the so-called Morlet wavelet (Gabor, 1946; Morlet et al., 1982), that is,

$$\xi(\mathbf{x}) = \left(e^{-2\pi i \mathbf{k}_0 \cdot \mathbf{x}} - c_0\right) e^{-\frac{\mathbf{x} \cdot \mathbf{x}}{2x_0^2}}, \quad (12)$$

where c_0 is a constant included to ensure that Equation 11 is met. The central wavenumber \mathbf{k}_0 is taken to be $\mathbf{k}_0 = (k_0, 0)$ and the quantity x_0 is a reference length scale, here taken to be the Rossby radius ($x_0 = 100$ km), viz. the central length scale of the mother wavelet. We will choose $k_0 = 1/x_0$, in which case the constant c_0 is quite small and generally ignored (i.e., $c_0 = 0$), a convention adopted in this paper. Plots of Equation 12 are found in Figure 4. Note that the Morlet mother wavelet consists of a wave of wavelength x_0 inside a Gaussian envelope of

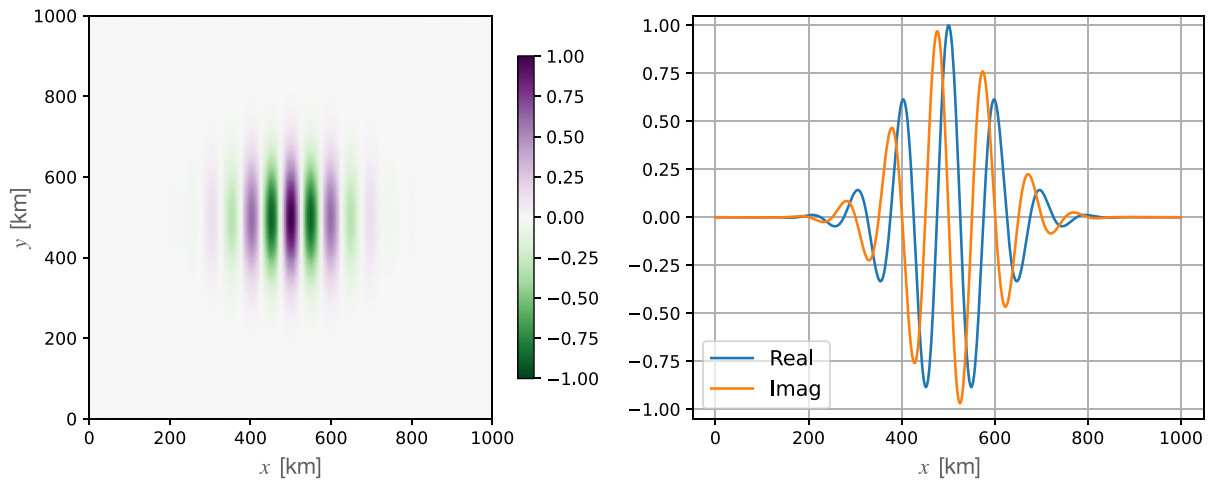


Figure 4. Structure of the mother Morlet wavelet Equation 12 for $c_0 = 0$. A contour plot of the real part of the mother Morlet wavelet is shown in the left panel. Zonal transects of the real and imaginary parts at $y = 500$ km appear in the right panel. The reference lengthscale is $x_0 = 100$ km.

decay scale $\sqrt{2}x_0$. Thus for $s = 1$ and $\phi = 0$, the wavelet coefficient produced by this transformation comments on the presence of the wavenumber $\mathbf{k}_0 = (k_0, 0)$ at location γ in the original data. Increasing the rotation angle ϕ and filtering returns information about the presence of the same wavelength at angle $-\phi$. Finally allowing s to vary modifies the filter so that the primary wavenumber of the filter is $k = 1/(sx_0)$. The Morlet wavelet coefficient can thus be thought of as a “local” Fourier transform at wavenumber $\mathbf{k}_0^T \cdot \mathbf{R}^{-1}(\phi)/s$, where the superscript T denotes a transpose. We note that Morlet wavelets are not orthonormal. However, this does not hinder our results as we are focused on continuous wavelet transforms.

From the properties of wavelets, it is possible to show they satisfy a generalized Parseval's equality (cf. Appendix A, Chen & Chu, 2017; Daubechies, 1992; Torrence & Compo, 1998), namely

$$\int_{\mathbf{x}} f(\mathbf{x})g(\mathbf{x})d\mathbf{x} = \frac{1}{C_{\Xi}} \int_{\phi} \int_s \int_{\gamma} \frac{\tilde{f}\tilde{g}^*}{s^3} d\gamma ds d\phi. \quad (13)$$

Note, if $f = g$, then the variance in f is captured via

$$\int_{\mathbf{x}} f^2(\mathbf{x})d\mathbf{x} = \frac{1}{C_{\Xi}} \int_{\phi} \int_s \int_{\gamma} \frac{\tilde{f}^*\tilde{f}}{s^3} d\gamma ds d\phi, \quad (14)$$

which identifies the quantity

$$\tilde{E}_S(\gamma, \phi, s) = \frac{1}{C_{\Xi}} \frac{\tilde{f}^*\tilde{f}}{s^3}, \quad (15)$$

as the energy density of f in wavelet space s and direction ϕ . In other words, Equation 15 gives a spectral energy estimate for f that belongs to location γ .

At this point, the scale factor in Equation 15, s , is non-dimensional. It is more traditional in fluid mechanics to discuss energy spectra in terms of wavenumber. As pointed out above, the effective wavenumber associated with s is $k = 1/(sx_0) = 1/s_0$, where the quantity s_0 has units of length. One can transform Equation 14 from s to s_0 space as

$$\int_{\mathbf{x}} f^2(\mathbf{x})d\mathbf{x} = \frac{1}{C_{\Xi}} \int_{\phi} \int_{s_0} \int_{\gamma} \frac{\tilde{f}^*\tilde{f}}{s_0^3} x_0^2 d\gamma ds_0 d\phi, \quad (16)$$

and finally to wavenumber, $k = 1/s_0$, space, ending with

$$\int_{\mathbf{x}} f^2(\mathbf{x})d\mathbf{x} = \frac{1}{C_{\Xi}} \int_{\phi} \int_k \int_{\gamma} \tilde{f}^*\tilde{f}x_0^2 k d\gamma dk d\phi. \quad (17)$$

If we now produce wavelet coefficients for the stream function and PV from time step n of our simulation, and manipulate them appropriately, we obtain

$$\tilde{E}_k^n(\gamma, \phi, k) = \frac{1}{C_{\Xi}} \mathcal{R} [(-\tilde{\psi}^*)\tilde{q}] x_0^2 k, \quad (18)$$

$$\tilde{Z}_k^n(\gamma, \phi, k) = \frac{1}{C_{\Xi}} \mathcal{R} \left[\frac{\tilde{q}^* \tilde{q}}{2} \right] x_0^2 k, \quad (19)$$

where $\mathcal{R}[\cdot]$ is the real part of the quantity \cdot , as a measure of energy and enstrophy density in wavelet transform space (cf. Uchida, Deremble, & Penduff, 2021; Vallis, 2006). Each value of \tilde{E}_k^n and \tilde{Z}_k^n is a random number (as they are associated with each realization of random eddies). Ensemble averaging those values where the members are snapshots at intervals of 30 days, returns an estimate of the energy spectrum as a function of wavenumber k in direction ϕ . The interval of 30 days ensures temporal decorrelation between the density estimates. The spatial locality of the mother wavelet permits the interpretation of $\tilde{E}_k(\gamma, \phi, k) = \overline{\tilde{E}_k^n(\gamma, \phi, k)}$ as the local energy spectrum at location γ . The same argument applies for enstrophy.

3. Results

We have opted for this work to calculate the wavelet coefficients explicitly, rather than by the frequently used Fourier transform method, in view of our eventual interest in applications to realistic aperiodic and inhomogeneous settings, such as the North Atlantic basin. The wavelet transform appropriate to the angle ϕ was taken between $[0, -\pi]$ with the azimuthal resolution of $\pi/12$ radian ($=15^\circ$). The sum of the product of the wavelet and the data spatially integrated is the wavelet coefficient at the location γ . In what follows, we consider the quasi two-dimensional flow in the top layer ($j = 1$).

3.1. Spectra Over the Entire Domain

We examine and intercompare the wavelet and Fourier wavenumber spectra and spectral flux over the entire domain in this section. As the simulated domain is doubly periodic and on a uniform grid, it is an ideal case for the Fourier method; no windowing nor spatial interpolation are applied prior to taking the transform. Although one of the strengths of the wavelet approach is in negating the necessity of periodicity, we have chosen such an idealized configuration to test the wavelet method against the Fourier method where the latter would provide the “true” spectra.

While the scaling factor s provides flexibility in defining the wavelet wavenumber, as opposed to the Fourier approach where, to employ Fast Fourier Transform algorithms, the resolution is constrained to $1/L$ with L ($=1,000$ km) being the domain size, we start by computing the wavelet spectra at the center location $\gamma = \gamma_0 = (y_c, x_c) = (500, 500)$ km and use the same wavenumbers as the Fourier spectra (k_f). We see from Figure 5 that the agreement between the Fourier and wavelet method is excellent (red solid and black dashed curves, respectively) for both the energy and enstrophy spectra at scales above the dissipation scale.

We also show in Figure 5 a case where we arbitrarily increase the wavelet wavenumber resolution at scales larger than 50 km where the inverse cascade is expected (black dashed curve); we take $s_0 = [2\Delta x, \dots, 5x_0]$ monotonically spaced with 30 increments, which is trimmed for scales smaller than 50 km, and concatenate this with the Fourier length scales below 50 km. Features at the lowest wavenumbers (i.e., largest spatial scales) are better captured compared to the red solid and black dotted curves in Figure 5 where the Fourier wavenumber resolution is low. This is beneficial as the scales of interest in the oceanographic context are often length scales about and larger than the Rossby radius, associated with mesoscale eddies (Chelton et al., 1998, 2011). The enstrophy spectra are slightly steeper than k^{-1} at scales below the Rossby radius (Figure 5b), which is consistent with the KE spectral slope also being steeper than -3 . We attribute the steeper slope to the excessive PV variance introduced by the stochastic forcing cascading downscale (cf. Figure 6b) and the sporadic emergence of coherent structures (e.g., Figure 3 left panel, Benzi et al., 1988; Maltrud & Vallis, 1991). While the spectral slopes do not match exactly to what is expected from the inertial range theory, it is known that the spectral slopes are sensitive to the model configuration of forcing and dissipation (Maltrud & Vallis, 1991), and this does not diminish the agreement between the Fourier and wavelet spectral estimates.

Using the wavelet transformation, we can also diagnose the KE and enstrophy spectral flux as

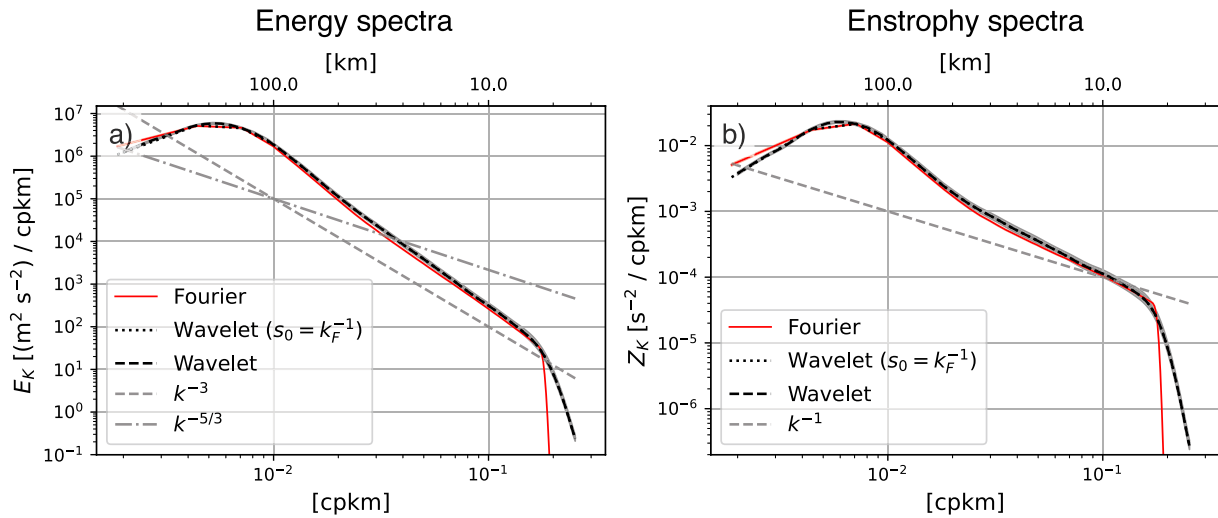


Figure 5. The isotropic (azimuthally integrated) energy and enstrophy wavenumber spectra of the top layer (a, b). For the wavelet approach, spectra at $\gamma = \gamma_0$ where the wavenumbers are identical to the Fourier wavenumbers ($s_0 = k_F^{-1}$; black dotted) and where the wavenumber resolution is increased at scales larger than 50 km (black dashed) are given. The wavenumber are shown in the lower x axes and corresponding lengthscale in the upper axes. The colored shadings indicate the 95% bootstrapped confidence interval and are shown for the Fourier spectra (red solid) and wavelet spectra with increased wavenumber resolution (black dashed) although the intervals are narrower than the curves themselves.

$$\bar{\epsilon}_k(\gamma, \phi, k) = -\frac{1}{C_\Psi} \int_{k > \kappa} \mathcal{R} \left[\overline{\tilde{u}^*(\mathbf{u} \cdot \nabla \mathbf{u})} + \overline{\tilde{v}^*(\mathbf{u} \cdot \nabla v)} \right] x_0^2 \kappa \, d\kappa, \quad (20)$$

$$\bar{\eta}_k(\gamma, \phi, k) = -\frac{1}{C_\Psi} \int_{k > \kappa} \mathcal{R} \left[\overline{\tilde{q}^*(\mathbf{u} \cdot \nabla q)} \right] x_0^2 \kappa \, d\kappa, \quad (21)$$

where negative values imply an inverse cascade toward larger scales and positive values a forward cascade toward smaller scales (Arbic et al., 2013; Khatri et al., 2018).

Comparisons of the spectral fluxes computed using wavelets at a single point (black), standard Fourier spectra (red) and spatial averages of point-wise wavelets (blue) are shown in Figures 6a and 6b. All approaches clearly indicate a broad forward enstrophy cascade range at scales smaller than the forcing scale/Rossby radius. Similarly, there is general agreement on the existence of an inverse energy cascade in the limited range of scales larger than the forcing scale. The lower panels in Figure 6 show the azimuthally integrated spectral transfers, that is, the integrand of Equations 20 and 21.

In contrast to calculations of the spectra themselves shown in Figure 5, the spectral fluxes computed from wavelet data taken at a single spatial point differ significantly from the global Fourier estimates. As described below, the wavelet spectral flux estimates are highly sensitive to the amount of spatial and temporal averaging employed, despite the homogeneity and statistical stationarity of the flow field. This sensitivity arises because the flux is the transfer cumulatively integrated from the largest wavenumbers toward smaller wavenumbers (i.e., Equation 20) so values at high wavenumbers can have a substantial effect on the flux at low wavenumbers.

The 95% bootstrapped confidence intervals, computed by randomly re-sampling spectral quantities 9,999 times, are shown by shading in Figure 6. In all cases, single-point wavelet flux and transfer estimates are highly uncertain, while Fourier estimates are not.

We argue this dependency on averaging is associated with the fact that the wavelet estimate of the spectral transfer only incorporates spatially local information while the Fourier approach effectively yields a domain-averaged estimate. Namely, the global two-point correlation function, stemming from the assumption of homogeneity in the Fourier approach, acts as a spatial averaging operator (cf. Uchida, Jamet, et al., 2021). For this setting, this assumption is valid, hence the superior performance in flux estimation of the Fourier approach. Note, however, that the transfer estimates emerging from the wavelet approach, while noisy, do largely agree with those of the Fourier approach. It is in the integration of the transfers where initial noise in the estimates can result in an erroneous outcome (compare black and blue curves in Figure 6d).

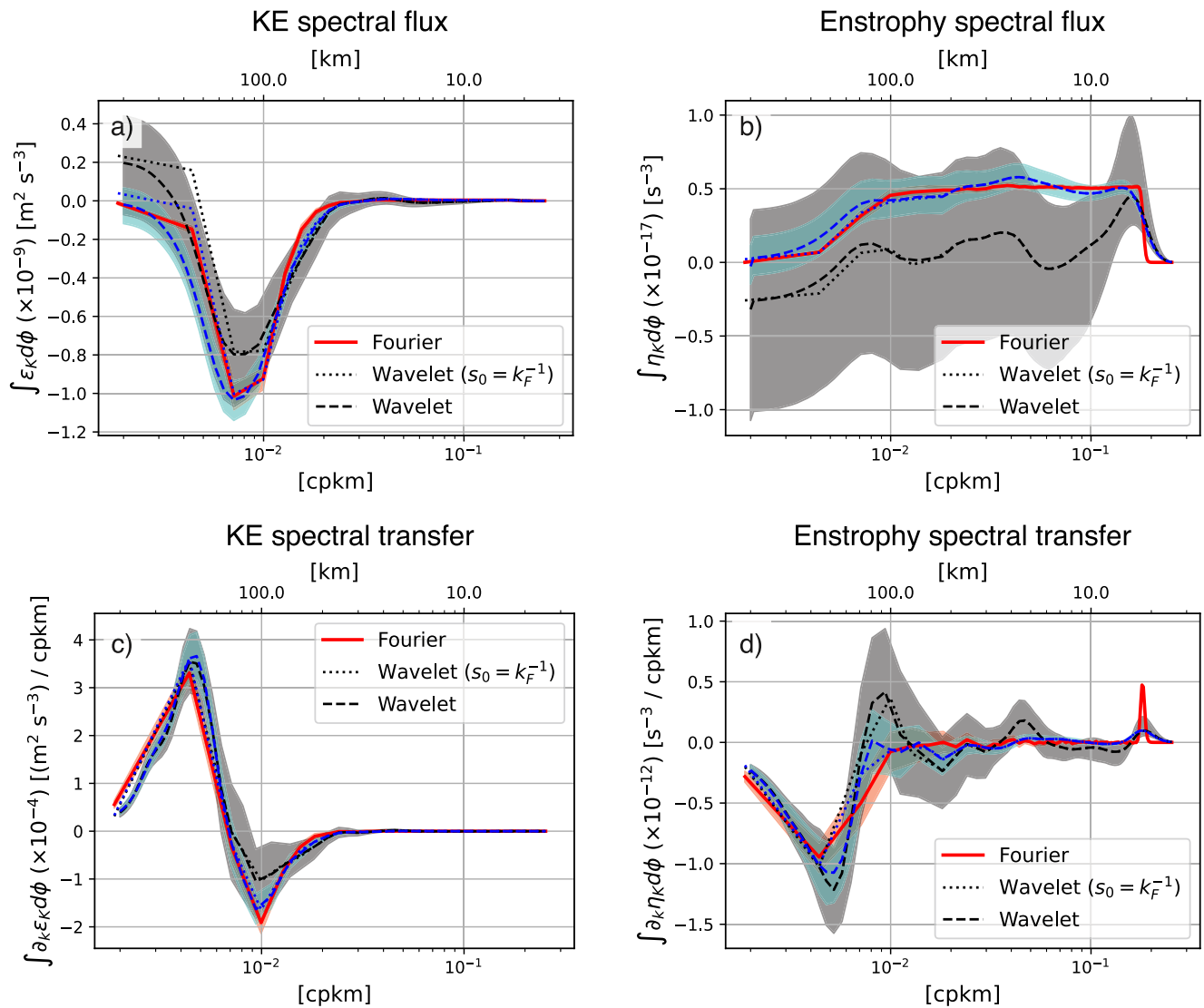


Figure 6. The isotropic (azimuthally integrated) kinetic energy and enstrophy wavenumber spectral flux (a, b) and transfer (c, d), respectively. The Fourier method is shown in red and the wavelet approach at $\gamma = \gamma_0$ with wavenumbers identical to the Fourier wavenumbers in dotted ($s_0 = k_F^{-1}$) and the case with increased wavenumber resolution at smaller wavenumbers in dashed curves, respectively. The black curves show the wavelet flux and transfer at $\gamma = \gamma_0$, while the blue curves show them averaged over the 101 locations ($\langle \varepsilon_K \rangle$, $\langle \eta_K \rangle$). The colored shadings indicate the 95% bootstrapped confidence interval and are shown for the Fourier spectra (red solid) and wavelet spectra with increased wavenumber resolution (black and blue dashed curves). The wavenumber is shown in the lower x axes and corresponding lengthscale in the upper axes.

The expectation is that if we were to take the explicit wavelet transform at every single grid point, the spatial average of the wavelet spectral flux would converge to the Fourier approach. We examined this by estimating the wavelet spectral flux and transfer at every five grid points in the diagonal direction (i.e., every ~ 14 km) up to 125 grid points apart (~ 280 km) from the center point (101 locations in total along $y - y_c = \pm(x - x_c)$). The spatial average of them shown as blue curves in Figure 6 all come closer to the Fourier estimate than the black curves. Comparisons of the domain averaged wavelet estimates to those derived via standard Fourier approach, both in their mean and confidence intervals, significantly improve when averaged over 101 locations ($\langle \varepsilon_K \rangle$, $\langle \eta_K \rangle$) where $\langle \cdot \rangle$ is the averaging operator over 101 locations; blue curves in Figures 6b and 6d). The Fourier and wavelet spectral transfer and flux also no longer differ at the 95% confidence interval.

We also exhibit the angular orientation of the spectral flux, which the wavelet approach can extract via its dependence on the angle ϕ (Figure 7). The flux shown in Figures 6a and 6b as blue dashed curves are the azimuthal integration of angle-dependent fluxes exhibited in Figure 7. As the simulated QG flow is configured to be isotropic, the

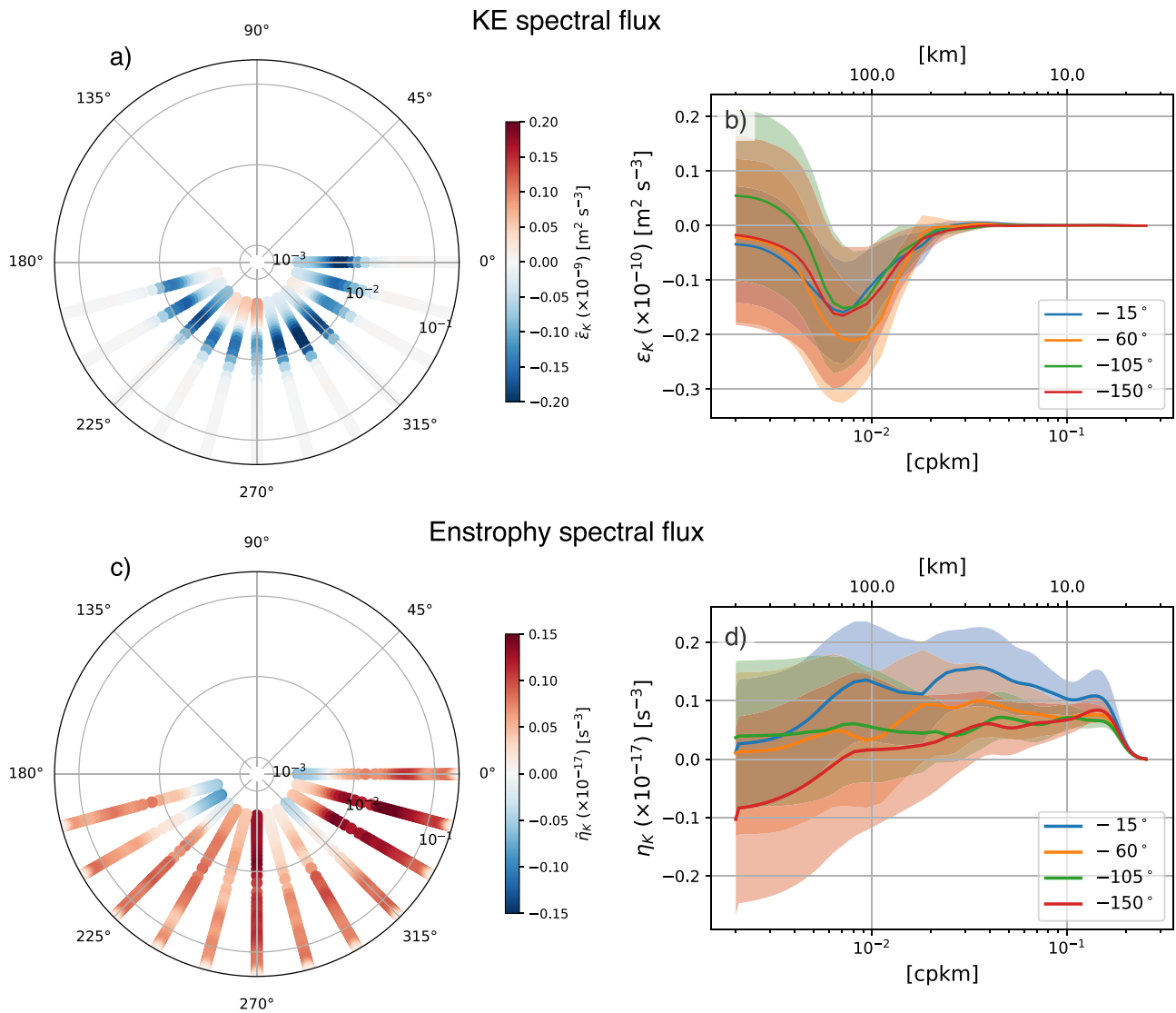


Figure 7. The angular dependence of the kinetic energy and enstrophy spectral flux from the wavelet approach plotted radially averaged over the 101 locations ($\langle \tilde{\epsilon}_k(\phi, k) \rangle, \langle \tilde{\eta}_k(\phi, k) \rangle$); a, c). The radial axes are the wavenumbers in logarithmic scaling with the increased wavenumber resolution. The fluxes are symmetric about the origin so we only show for angles $[0, -\pi)$. The 95% boot-strapped confidence intervals are given for four arbitrary angles (b, d).

anisotropy seen in the spectral flux are statistically insignificant within the 95% boot-strapped confidence interval; the KE flux exhibits an inverse cascade and enstrophy flux a forward cascade across all angles (Figures 7b and 7d).

We are thus led to be cautious interpreting single-point wavelet spectral calculations when applied to what might be termed higher order quantities, like spectral flux. However, we also point out this is a sword that cuts in both directions. The accuracy of the Fourier flux estimates depends strongly on their area-wide integrative effect in this homogeneous setting. Were the flow not homogeneous, the integrative character of the Fourier approach would obscure the meaning of the result.

3.2. Spectra Over a Non-Periodic Subdomain

We now examine the spectra taken over the subdomain given by $y = 200\text{--}800$ and $x = 200\text{--}800$ km in anticipation of realistic data where periodicity is never satisfied. As the data are no longer periodic, the Fourier approach requires the data to be windowed. This will highlight the strength of the locality in the wavelet approach where windowing of the data is unnecessary. Prior to taking the Fourier transforms, we applied Hann windows (Arbic et al., 2013; Uchida et al., 2017; Uchida, Jamet, et al., 2021) and then corrected for their amplitude. Comparing

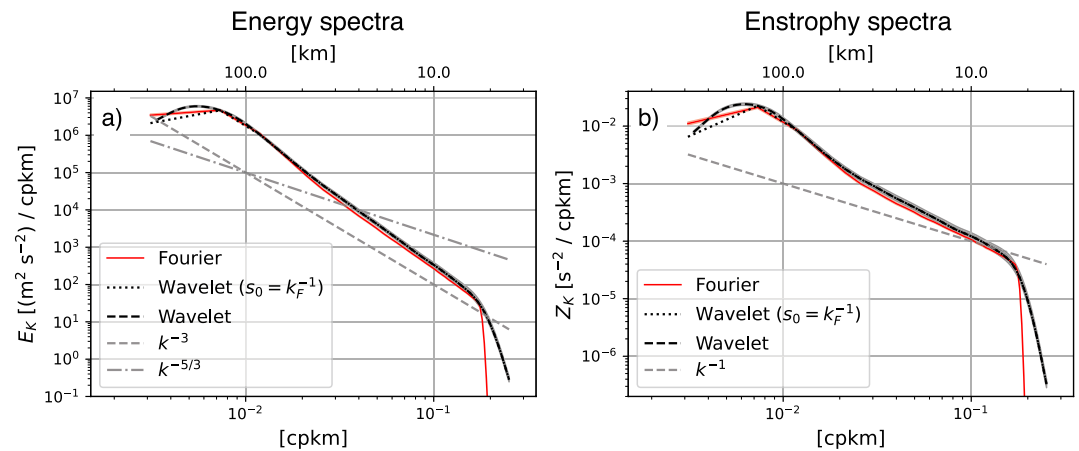


Figure 8. Same as Figure 5 but for the subdomain of $y = 200\text{--}800$ and $x = 200\text{--}800$ km. The confidence intervals are again narrower than the curves themselves.

Figures 5 and 8, we see that the spectral estimates are still robust. The low resolution at lower wavenumbers from the Fourier method makes it difficult to detect the spectral shape at scales above ~ 100 km due to the domain size being small; there are only two wavenumber points at scales larger than the Rossby radius (red curves in Figure 8). The wavelet approach, on the other hand through its flexibility in s , still captures a smooth spectral estimate; the scaling for the wavelet approach was adjusted to $s_0 = [2\Delta x, \dots, 3x_0]$ over 30 monotonic increments in order to account for the smaller domain and then replaced by the Fourier wavenumber at scales smaller than 50 km.

Regarding the spectral transfer, the Fourier approach is significantly affected by the tapering at the lowest wavenumbers (red curves in Figures 6c, 6d, 9c, and 9d) but the wavelet approach is still able to capture the change in sign in its curvature (blue dashed curves in Figures 6c, 6d, 9c, and 9d). The enstrophy spectral flux and transfer tend to be particularly sensitive to the local nature of wavelet transforms. Similar to Figure 6, we see a significant improvement in the wavelet estimates both in their mean and confidence intervals when averaged over 101 locations, particularly for enstrophy ($\langle \tilde{\eta}_k \rangle$; blue curves in Figures 9b and 9d).

4. Conclusions and Discussion

In this study, we have described and documented a wavelet-based technique for spectral analyses in an oceanographic context. The wavelet approach employed here, through its dependence on a scale parameter s , returns effectively a one-dimensional (1D) spectral estimate, and its incorporating of two-dimensional data allows for information regarding local anisotropies through its angular dependency ϕ (Figure 7).

We have demonstrated its utility by applying it to a doubly periodic, two-layer, QG simulation. The flow analyzed in this study is highly idealized being spatially isotropic and homogeneous in the horizontal dimensions. The idealized setting, however, is expected to yield known spectral cascades, so it can be used as a test bed for the wavelet approach. The agreement between the wavelet and Fourier approach, particularly for the spectra (Figures 5 and 8), encourages the usage of wavelets with its additional strengths of being able to capture the local features of the flow. While numerically efficient algorithms exist to take the wavelet transform (coined as Fast Wavelet Transforms; e.g., Beylkin et al., 1991), they face the same conundrum as FFTs requiring: (a) periodic boundary conditions and (b) filling in missing data points. We have, therefore, taken the approach of explicitly computing the wavelet transform Equation 7, which negates the two necessities and will benefit realistic settings such as the North Atlantic basin. The robustness of the spectra is comforting, but we also emphasize the need for caution when computing higher-order spectral quantities, like spectral fluxes, which involve spatial derivatives. The disagreement arises from the local nature of wavelets; the Fourier method incorporates spatially global information and hence can be thought as a spatial average of spectral estimates. This is evident from the fact that upon spatially averaging the wavelet spectral transfer over multiple locations, the confidence interval improved and its mean converged toward the Fourier estimate.

Our work is complementary to a growing list of literature on spectral methods alternative to the Fourier approach: Aluie et al. (2018), Sadek and Aluie (2018), Schubert et al. (2020), Storer et al. (2022), and Contreras et al. (2022) where they use a spatial filter to examine the KE spectra and cross-scale transfer, Lindborg (2015), Balwada

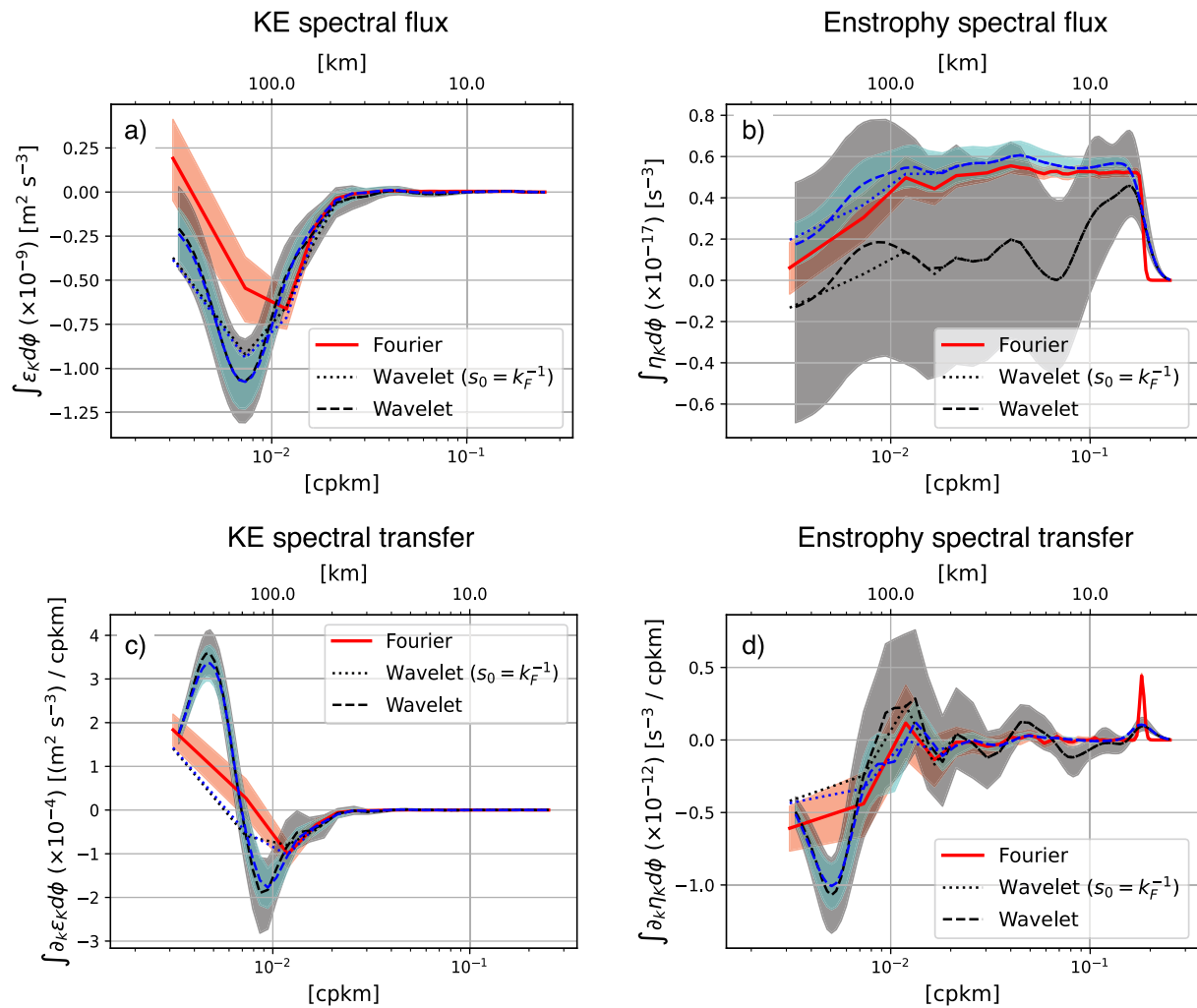


Figure 9. Same as Figure 6 but for the subdomain of $y = 200\text{--}800$ and $x = 200\text{--}800$ km.

et al. (2016, 2022), LaCasce (2016), Poje et al. (2017), and Pearson et al. (2020) where they implement structure functions, Jamet et al. (2020) where they employ the Green's function, and Uchida, Jamet, et al. (2021) where they use Empirical Orthogonal Functions. Barkan et al. (2021) and Srinivasan et al. (2022) apply the filtering method in both the spatiotemporal dimensions. Liang and Anderson (2007), Liang (2016), and Yang et al. (2021) are also interesting attempts in implementing a multiscale window transform to examine the energy exchange across spatiotemporal scales by decomposing the flow with a set of orthogonal windows. Here, we have documented the wavelet-based cross-scale energetics in the spectral context. While the form of the Parseval's equality will slightly change, namely in the power of scaling s , the wavelet method can also be extended to estimating frequency-wavenumber spectra (e.g., Torres et al., 2018; Uchida et al., 2019); this will allow us to decompose the balanced and unbalanced motions in non-periodic settings.

Appendix A: Parseval's Equality

In this appendix, we review the Parseval's equality for two-dimensional wavelet transforms (Chen & Chu, 2017; Daubechies, 1992; Mallat, 1999; Torrence & Compo, 1998), that is,

$$\int f g \, d\mathbf{x} = \frac{1}{C_{\Xi}} \iiint \tilde{f} \tilde{g}^* \frac{1}{s^3} \, d\gamma ds d\phi. \quad (\text{A1})$$

Using Equation 9, the right-hand side can be expanded as

$$\begin{aligned} \iiint \tilde{f} \tilde{g}^* \frac{1}{s^3} d\gamma ds d\phi &= \iiint \frac{1}{s^5} \int_x f(\mathbf{x}) \xi^* \left(\mathbf{R}^{-1} \cdot \left(\frac{\mathbf{x} - \boldsymbol{\gamma}}{s} \right) \right) d\mathbf{x} \int_x g^*(\boldsymbol{\chi}) \xi \left(\mathbf{R}^{-1} \cdot \left(\frac{\boldsymbol{\chi} - \boldsymbol{\gamma}}{s} \right) \right) d\boldsymbol{\chi} d\gamma ds d\phi \\ &= \int_x \int_x f g^* \iiint \frac{1}{s^5} \xi^* \left(\mathbf{R}^{-1} \cdot \left(\frac{\mathbf{x} - \boldsymbol{\gamma}}{s} \right) \right) \xi \left(\mathbf{R}^{-1} \cdot \left(\frac{\boldsymbol{\chi} - \boldsymbol{\gamma}}{s} \right) \right) d\gamma ds d\phi d\mathbf{x} d\boldsymbol{\chi}. \end{aligned} \quad (\text{A2})$$

Now, consider the wavelet transform of the Dirac delta function

$$\begin{aligned} \tilde{\delta} &= \int_x \delta(\mathbf{x} - \mathbf{x}') \frac{1}{s} \xi^* \left(\mathbf{R}^{-1} \cdot \left(\frac{\mathbf{x} - \boldsymbol{\gamma}}{s} \right) \right) d\mathbf{x} \\ &= \frac{1}{s} \xi^* \left(\mathbf{R}^{-1} \cdot \left(\frac{\mathbf{x}' - \boldsymbol{\gamma}}{s} \right) \right). \end{aligned} \quad (\text{A3})$$

Hence, the inverse wavelet transform becomes

$$\begin{aligned} \delta &= \frac{1}{C_{\Xi}} \iiint \tilde{\delta} \frac{1}{s^4} \xi \left(\mathbf{R}^{-1} \cdot \left(\frac{\mathbf{x} - \boldsymbol{\gamma}}{s} \right) \right) d\phi ds d\boldsymbol{\gamma} \\ &= \frac{1}{C_{\Xi}} \iiint \frac{1}{s^5} \xi^* \left(\mathbf{R}^{-1} \cdot \left(\frac{\mathbf{x}' - \boldsymbol{\gamma}}{s} \right) \right) \xi \left(\mathbf{R}^{-1} \cdot \left(\frac{\mathbf{x} - \boldsymbol{\gamma}}{s} \right) \right) d\phi ds d\boldsymbol{\gamma}. \end{aligned} \quad (\text{A4})$$

Plugging Equation A4 into Equation A2 yields

$$\iiint \tilde{f} \tilde{g}^* \frac{1}{s^3} d\gamma ds d\phi = C_{\Xi} \int_x f g^* d\mathbf{x}, \quad (\text{A5})$$

and we obtain Equation A1.

Data Availability Statement

The wavelet transforms were taken using the `xwavelet` Python package (Uchida & Dewar, 2022) and Fourier transforms using the `xrfft` Python package (Uchida et al., 2022). The `pyqg` model is available through Github (Abernathey et al., 2022). Jupyter notebooks used to run the `pyqg` simulation and conduct analyses are available via Github (Uchida, 2023).

References

- Abernathey, R. P., Ross, A., Jansen, M., Li, Z., Poulin, F. J., Constantinou, N. C., et al. (2022). `pyqg`: Python quasigeostrophic model. [Software]. <https://doi.org/10.5281/zenodo.6563667>
- Ajayi, A., Le Sommer, J., Chassignet, E., Molines, J., Xu, X., Albert, A., & Dewar, W. (2021). Diagnosing cross-scale kinetic energy exchanges from two submesoscale permitting ocean models. *Journal of Advances in Modeling Earth Systems*, 13(6), e2019MS001923. <https://doi.org/10.1029/2019MS001923>
- Aluie, H., Hecht, M., & Vallis, G. (2018). Mapping the energy cascade in the North Atlantic Ocean: The coarse-graining approach. *Journal of Physical Oceanography*, 48(2), 225–244. <https://doi.org/10.1175/JPO-D-17-0100.1>
- Alvera-Azcárate, A., Barth, A., Bouallègue, Z. B., Rixen, M., & Beckers, J.-M. (2007). Forecast verification of a 3D model of the Mediterranean Sea. The use of discrete wavelet transforms and EOFs in the skill assessment of spatial forecasts. *Journal of Marine Systems*, 65(1–4), 460–483. <https://doi.org/10.1016/j.jmarsys.2005.09.015>
- Arbic, B. K., Polzin, K. L., Scott, R. B., Richman, J. G., & Shriver, J. F. (2013). On eddy viscosity, energy cascades, and the horizontal resolution of gridded satellite altimeter products. *Journal of Physical Oceanography*, 43(2), 283–300. <https://doi.org/10.1175/JPO-D-11-0240.1>
- Balwada, D., LaCasce, J. H., & Speer, K. G. (2016). Scale-dependent distribution of kinetic energy from surface drifters in the Gulf of Mexico. *Geophysical Research Letters*, 43(20), 10–856. <https://doi.org/10.1002/2016GL069405>
- Balwada, D., Xie, J.-H., Marino, R., & Feraco, F. (2022). Direct observational evidence of an oceanic dual kinetic energy cascade and its seasonality. *Science Advances*, 8(41), eabq2566. <https://doi.org/10.1126/sciadv.abq2566>
- Barkan, R., Srinivasan, K., Yang, L., McWilliams, J. C., Gula, J., & Vic, C. (2021). Oceanic mesoscale eddy depletion catalyzed by internal waves. *Geophysical Research Letters*, 48(18), e2021GL094376. <https://doi.org/10.1029/2021GL094376>
- Benzi, R., Patarnello, S., & Santangelo, P. (1988). Self-similar coherent structures in two-dimensional decaying turbulence. *Journal of Physics A: Mathematical and General*, 21(5), 1221–1237. <https://doi.org/10.1088/0305-4470/21/5/018>
- Beylkin, G., Coifman, R., & Rokhlin, V. (1991). Fast wavelet transforms and numerical algorithms I. *Communications on Pure and Applied Mathematics*, 44(2), 141–183. <https://doi.org/10.1002/cpa.3160440202>
- Capet, X., McWilliams, J. C., Molemaker, M. J., & Shechepetkin, A. F. (2008). Mesoscale to submesoscale transition in the California current system. Part I: Flow structure, eddy flux, and observational tests. *Journal of Physical Oceanography*, 38(1), 29–43. <https://doi.org/10.1175/2007JPO3671.1>
- Charney, J. G. (1971). Geostrophic turbulence. *Journal of the Atmospheric Sciences*, 28(6), 1087–1095. [https://doi.org/10.1175/1520-0469\(1971\)028<1087:GT>2.0.CO;2](https://doi.org/10.1175/1520-0469(1971)028<1087:GT>2.0.CO;2)

Acknowledgments

We thank the editor Stephen M. Griffies along with three anonymous reviewers who helped improve our manuscript. This study is a contribution to the “Assessing the Role of forced and internal Variability for the Ocean and climate Response in a changing climate” (ARVOR) project supported by the French “Les Enveloppes Fluides et l’Environnement” (LEFE) program. This work was supported via NSF Grants OCE-1829856, OCE-2023585, OCE-2123632 and the French “Make Our Planet Great Again” program managed by the Agence Nationale de la Recherche under the Programme d’Investissement d’Avenir, reference ANR-18-MPGA-0002. The latter two grants served as the primary support for T. Uchida and partially for Q. Jamet. A. Poje acknowledges support from the NSF Grant OCE-2123633. We would like to thank Edward Peirce and Kelly Hirai for maintaining the Florida State University cluster on which the simulations were run and data were analyzed.

- Chelton, D. B., DeSzoeke, R. A., Schlax, M. G., El Naggar, K., & Siwertz, N. (1998). Geographical variability of the first baroclinic rossby radius of deformation. *Journal of Physical Oceanography*, 28(3), 433–460. [https://doi.org/10.1175/1520-0485\(1998\)028<0433:GVOTFB>2.0.CO;2](https://doi.org/10.1175/1520-0485(1998)028<0433:GVOTFB>2.0.CO;2)
- Chelton, D. B., Schlax, M. G., & Samelson, R. M. (2011). Global observations of nonlinear mesoscale eddies. *Progress in Oceanography*, 91(2), 167–216. <https://doi.org/10.1016/j.pocean.2011.01.002>
- Chen, C., & Chu, X. (2017). Two-dimensional Morlet wavelet transform and its application to wave recognition methodology of automatically extracting two-dimensional wave packets from lidar observations in Antarctica. *Journal of Atmospheric and Solar-Terrestrial Physics*, 162, 28–47. <https://doi.org/10.1016/j.jastp.2016.10.016>
- Contreras, M., Renault, L., & Marchesiello, P. (2022). Understanding energy pathways in the gulf stream. *Journal of Physical Oceanography*, 53(3), 719–736. <https://doi.org/10.1175/JPO-D-22-0146.1>
- Daubechies, I. (1992). *Ten lectures on wavelets*. SIAM.
- Doglioli, A., Blanke, B., Speich, S., & Lapeyre, G. (2007). Tracking coherent structures in a regional ocean model with wavelet analysis: Application to Cape Basin eddies. *Journal of Geophysical Research*, 112(C5), C05043. <https://doi.org/10.1029/2006JC003952>
- Farge, M. (1992). Wavelet transforms and their applications to turbulence. *Annual Review of Fluid Mechanics*, 24(1), 395–458. <https://doi.org/10.1146/annurev.fl.24.010192.002143>
- Gabor, D. (1946). Theory of communication. Part I: The analysis of information. *Journal of the Institution of Electrical Engineers-Part III: Radio and Communication Engineering*, 93(26), 429–441. <https://doi.org/10.1049/ji-3-2.1946.0074>
- Horbury, T. S., Forman, M., & Oughton, S. (2008). Anisotropic scaling of magnetohydrodynamic turbulence. *Physical Review Letters*, 101(17), 175005. <https://doi.org/10.1103/PhysRevLett.101.175005>
- Jamet, Q., Ajayi, A., Le Sommer, J., Penduff, T., Hogg, A., & Dewar, W. (2020). On energy cascades in general flows: A Lagrangian application. *Journal of Advances in Modeling Earth Systems*, 12(12), e2020MS002090. <https://doi.org/10.1029/2020MS002090>
- Jamet, Q., Deremble, B., Wienders, N., Uchida, T., & Dewar, W. K. (2021). On wind-driven energetics of subtropical gyres. *Journal of Advances in Modelling Earth Systems*, 13(4), e2020MS002329. <https://doi.org/10.1029/2020MS002329>
- Katul, G. G., & Parlange, M. B. (1995). The spatial structure of turbulence at production wavenumbers using orthonormal wavelets. *Boundary-Layer Meteorology*, 75(1), 81–108. <https://doi.org/10.1007/BF00721045>
- Khatri, H., Sukhatme, J., Kumar, A., & Verma, M. K. (2018). Surface ocean enstrophy, kinetic energy fluxes, and spectra from satellite altimetry. *Journal of Geophysical Research: Oceans*, 123(5), 3875–3892. <https://doi.org/10.1029/2017JC013516>
- Kolmogorov, A. (1941). The local structure of turbulence in incompressible viscous fluid for very large Reynolds numbers. *C R Academy of Sciences URSS*, 30, 301–305.
- LaCasce, J. (2016). Estimating Eulerian energy spectra from drifters. *Fluids*, 1(4), 33. <https://doi.org/10.3390/fluids1040033>
- Liang, X. S. (2016). Canonical transfer and multiscale energetics for primitive and quasigeostrophic atmospheres. *Journal of the Atmospheric Sciences*, 73(11), 4439–4468. <https://doi.org/10.1175/JAS-D-16-0131.1>
- Liang, X. S., & Anderson, D. G. (2007). Multiscale window transform. *Multiscale Modeling and Simulation*, 6(2), 437–467. <https://doi.org/10.1137/06066895x>
- Lindborg, E. (2015). A Helmholtz decomposition of structure functions and spectra calculated from aircraft data. *Journal of Fluid Mechanics*, 762, R4. <https://doi.org/10.1017/jfm.2014.685>
- Mallat, S. (1999). *A wavelet tour of signal processing*. Elsevier.
- Maltrud, M., & Vallis, G. (1991). Energy spectra and coherent structures in forced two-dimensional and beta-plane turbulence. *Journal of Fluid Mechanics*, 228, 321–342. <https://doi.org/10.1017/S0022112091002720>
- Morlet, J., Arens, G., Fourgeau, E., & Glard, D. (1982). Wave propagation and sampling theory—Part I: Complex signal and scattering in multi-layered media. *Geophysics*, 47(2), 203–221. <https://doi.org/10.1190/1.1441328>
- Nastrom, G., & Gage, K. (1983). A first look at wavenumber spectra from GASP data. *Tellus*, 35(5), 383–388. <https://doi.org/10.1111/j.1600-0870.1983.tb00213.x>
- Pearson, J., Fox-Kemper, B., Pearson, B., Chang, H., Haus, B. K., Horstmann, J., et al. (2020). Biases in structure functions from observations of submesoscale flows. *Journal of Geophysical Research: Oceans*, 125(6), e2019JC015769. <https://doi.org/10.1029/2019JC015769>
- Perrier, V., Philipovitch, T., & Basdevant, C. (1995). Wavelet spectra compared to Fourier spectra. *Journal of Mathematical Physics*, 36(3), 1506–1519. <https://doi.org/10.1063/1.531340>
- Poje, A. C., Özgökmen, T. M., Bogucki, D. J., & Kirwan, A. (2017). Evidence of a forward energy cascade and Kolmogorov self-similarity in submesoscale ocean surface drifter observations. *Physics of Fluids*, 29(2), 020701. <https://doi.org/10.1063/1.4974331>
- Sadek, M., & Aluie, H. (2018). Extracting the spectrum of a flow by spatial filtering. *Physical Review Fluids*, 3(12), 124610. <https://doi.org/10.1103/PhysRevFluids.3.124610>
- Schubert, R., Gula, J., Greatbatch, R. J., Baschek, B., & Biastoch, A. (2020). The submesoscale kinetic energy cascade: Mesoscale absorption of submesoscale mixed layer eddies and frontal downscale fluxes. *Journal of Physical Oceanography*, 50(9), 2573–2589. <https://doi.org/10.1175/JPO-D-19-0311.1>
- Scott, R., & Wang, F. (2005). Direct evidence of an oceanic inverse kinetic energy cascade from satellite altimetry. *Journal of Physical Oceanography*, 35(9), 1650–1666. <https://doi.org/10.1175/JPO2771.1>
- Srinivasan, K., Barkan, R., & McWilliams, J. C. (2022). A forward energy flux at submesoscales driven by frontogenesis. *Journal of Physical Oceanography*, 53(1), 287–305. <https://doi.org/10.1175/JPO-D-22-0001.1>
- Stammer, D. (1997). Global characteristics of ocean variability estimated from regional TOPEX/POSEIDON altimeter measurements. *Journal of Physical Oceanography*, 27(8), 1743–1769. [https://doi.org/10.1175/1520-0485\(1997\)027<1743:gcoove>2.0.co;2](https://doi.org/10.1175/1520-0485(1997)027<1743:gcoove>2.0.co;2)
- Storer, B. A., Buzzicotti, M., Khatri, H., Griffies, S. M., & Aluie, H. (2022). Global energy spectrum of the general oceanic circulation. *Nature Communications*, 13(1), 5314. <https://doi.org/10.1038/s41467-022-33031-3>
- Taylor, G. (1938). The spectrum of turbulence. *Proceedings of the Royal Society of London*, A1(164), 476–490. <https://doi.org/10.1098/rspa.1938.0032>
- Thomson, R. E., & Emery, W. J. (2014). *Data analysis methods in physical oceanography*. Newnes.
- Torrence, C., & Compo, G. P. (1998). A practical guide to wavelet analysis. *Bulletin of the American Meteorological Society*, 79(1), 61–78. [https://doi.org/10.1175/1520-0477\(1998\)079<0061:APGTWA>2.0.CO;2](https://doi.org/10.1175/1520-0477(1998)079<0061:APGTWA>2.0.CO;2)
- Torres, H. S., Klein, P., Menemenlis, D., Qiu, B., Su, Z., Wang, J., et al. (2018). Partitioning ocean motions into balanced motions and internal gravity waves: A modeling study in anticipation of future space missions. *Journal of Geophysical Research: Oceans*, 123(11), 8084–8105. <https://doi.org/10.1029/2018jc014438>
- Uchida, T. (2023). Wavelet: Theory. Jupyter notebook repository for wavelet-based spectral analyses using QG outputs [Software]. <https://doi.org/10.5281/zenodo.5757149>

- Uchida, T., Abernathey, R. P., & Smith, K. S. (2017). Seasonality of eddy kinetic energy in an eddy permitting global climate model. *Ocean Modelling*, 118, 41–58. <https://doi.org/10.1016/j.ocemod.2017.08.006>
- Uchida, T., Balwada, D., Abernathey, R. P., McKinley, G., Smith, S., & Levy, M. (2019). The contribution of submesoscale over mesoscale eddy iron transport in the open southern ocean. *Journal of Advances in Modeling Earth Systems*, 11(12), 3934–3958. <https://doi.org/10.1029/2019MS001805>
- Uchida, T., Deremble, B., & Penduff, T. (2021). The seasonal variability of the ocean energy cycle from a quasi-geostrophic double gyre ensemble. *Fluids*, 6(6), 206. <https://doi.org/10.3390/fluids6060206>
- Uchida, T., & Dewar, W. K. (2022). xwavelet: Wavelet transforms for xarray data [Software]. <https://doi.org/10.5281/zenodo.6022738>
- Uchida, T., Jamet, Q., Poje, A., & Dewar, W. K. (2021). An ensemble-based eddy and spectral analysis, with application to the Gulf Stream. *Journal of Advances in Modeling Earth Systems*, 14(4), e2021MS002692. <https://doi.org/10.1029/2021MS002692>
- Uchida, T., Rokem, A., Squire, D., Nicholas, T., Abernathey, R. P., Soler, S., et al. (2022). xrft: Fourier transforms for xarray data [Software]. <https://doi.org/10.5281/zenodo.1402635>
- Vallis, G. (2006). Atmospheric and oceanic fluid dynamics.
- Vasilyev, O. V., & Paolucci, S. (1997). A fast adaptive wavelet collocation algorithm for multidimensional PDEs. *Journal of Computational Physics*, 138(1), 16–56. <https://doi.org/10.1006/jcph.1997.5814>
- Xu, Y., & Fu, L.-L. (2011). Global variability of the wavenumber spectrum of oceanic mesoscale turbulence. *Journal of Physical Oceanography*, 41(4), 802–809. <https://doi.org/10.1175/2010JPO4558.1>
- Xu, Y., & Fu, L.-L. (2012). The effects of altimeter instrument noise on the estimation of the wavenumber spectrum of sea surface height. *Journal of Physical Oceanography*, 42(12), 2229–2233. <https://doi.org/10.1175/JPO-D-12-0106.1>
- Yaglom, A. M. (2004). *An introduction to the theory of stationary random functions*. Mansfield Centre, Martino Publishing.
- Yang, Y., McWilliams, J. C., San Liang, X., Zhang, H., Weisberg, R. H., Liu, Y., & Menemenlis, D. (2021). Spatial and temporal characteristics of the submesoscale energetics in the Gulf of Mexico. *Journal of Physical Oceanography*, 51(2), 475–489. <https://doi.org/10.1175/JPO-D-20-0247.1>